Modeling and numerical simulations of Brownian rodlike particles with anisotropic translational diffusion

Hamza Issa, Giovanniantonio Natale, Gilles Ausias, Julien Férec

Modeling and numerical simulations of Brownian rodlike particles with anisotropic translational diffusion

Hamza Issa
Univ. Bretagne Sud, UMR CNRS 6027, IRDL, F-56100 Lorient, France
and Department of Chemical and Petroleum Engineering, Schulich School of Engineering, University of Calgary, Canada T2N 1N4

Giovanniantonio Natale
Department of Chemical and Petroleum Engineering, Schulich School of Engineering, University of Calgary, Canada T2N 1N4

Gilles Ausias
Univ. Bretagne Sud, UMR CNRS 6027, IRDL, F-56100 Lorient, France

Julien Férec
Univ. Bretagne Sud, UMR CNRS 6027, IRDL, F-56100 Lorient, France

(Received 12 September 2022; accepted 23 February 2023; published 24 March 2023)

A new kinetic macromodel based on moments of the probability distribution function is proposed to investigate the flow of rodlike Brownian particle suspensions. The rods concentration-orientation coupling is taken into account. A numerical study is presented for rods through the planar channel, with and without introducing a circular obstacle which develops a nonhomogeneous flow. To verify this macromodel, the results are compared with the solution of the associated Fokker-Planck equation taking into consideration an anisotropic translational diffusion tensor. This tensor depends on the local orientation of the rod. Low (smaller than 10^3) Brownian translational Peclet number causes rod migrations across the flow streamlines.

DOI: 10.1103/PhysRevFluids.8.033302

I. INTRODUCTION

Mechanical, thermal, or electrical properties are influenced significantly by the concentration and orientation distributions of nanoparticles in composite materials. Thus, predicting and controlling the concentration and orientation state of particle suspensions is critical for designing a successful manufacturing process of advanced materials [1–3].

Researchers have theoretically studied the evolution of the orientation of anisotropic particles homogeneously suspended during flow. Jeffery [4] derived the equation of motion of one isolated, inertialess, and axisymmetric particle in a Newtonian fluid with a uniform velocity gradient. When a dilute fiber suspension is exposed to a constant shear flow, fiber tends to align in the flow direction [5,6]. Folgar and Tucker [7] modified Jeffery's equation by introducing a scalar diffusion term to capture phenomenologically the interactions between non-Brownian particles in nondilute regimes. According to additional research, various perturbations inherent in flowing channels can have an impact on the reproducibility and endurance of rotations. Small deviations from a perfect axisymmetric rod shape, for example, can result in doubly periodic and chaotic orbits, which have been investigated both theoretically and experimentally [8–10]. Jeffery's orbits are perturbed by

the proximity of channel walls [11–15], inertia [10], and the viscoelasticity of the shearing fluid [16,17]. The Fokker-Planck equation (FP) for Brownian particles is derived from the work of Kirkwood and Auer [18] by Doi and Edwards [19]. Rheo-optical techniques have been used to measure rod distributions [20,21], and these results were compared to theoretical expectations and Brownian dynamics simulations [22–25]. Brownian fluctuations and their effect on orbits of individual Brownian rods in a microchannel flow have been studied theoretically [26]. In both the spatial and configurational spaces, some numerical strategies have been developed to solve the Fokker-Planck equation directly [27–33]. Park and Park [34] and Férec *et al.* [35] provided a thorough reviews of the fundamentals and numerical simulations for predicting fiber orientation during the injection molding of polymer composites.

When dispersed in a Newtonian liquid, isolated particles may exhibit cross-stream migration. Schiek and Shaqfeh [36] considered fiber migration across streamlines in a suspension under a plane Poiseuille flow in the weak flow limit, such that Brownian motion strongly affects the fiber position and orientation. At steady state, the center-of-mass distribution of fibers shows a net migration of fibers away from the center of the channel and toward the channel walls. Nitsche and Hinch [37] addressed the cross-stream migration of rigid rods undergoing diffusion and advection in a parabolic flow between flat plates. Results are obtained from using a finite-difference scheme for the solution of the Fokker-Planck equation. The results indicate that rods migrate toward the walls and toward the higher shear zone. Park *et al.* [38] used a kinetic theory to study the cross-stream migration of a rigid polymer undergoing rectilinear flow in the vicinity of a wall. In a simple shear flow, polymers migrate away from the wall, while in a pressure-driven flow, the center-of-mass distribution has an off-center maximum. This is because of the competition between the hydrodynamic interactions with the wall and the anisotropic diffusivity induced by the inhomogeneous flow field. Sharaf *et al.* [39] established that Brownian motion plays a significant role in the deposition of nanoparticles on the channel walls at low Reynolds number.

Solving a multidimensional Fokker-Planck equation has high computational costs. Developing an equivalent kinetic macromodel is a strategy to render the numerical solution of detailed physics overall more accessible. There is a large amount of published literature showing the use of macromodels for predicting particle orientation or concentration. Advani and Tucker [40] used a set of even-order tensors related to the coefficients of a Fourier series expansion of the probability distribution function to describe fiber orientation in suspensions containing short rigid fibers. Phillips *et al.* [41] proposed a constitutive equation for computing particle concentration and velocity fields in concentrated monomodal, spherical suspensions. Shapley *et al.* [42] compared the predictions of several models of particle migration to laser Doppler velocimetry measurements in various concentrated suspensions of noncolloidal spheres in a Couette flow. The models predict the observed macroscopic shear rate and concentration profiles well at moderate bulk particle concentration but diverge from one another at high concentrations. These models are either used to predict the orientation or the concentration, without studying the correlation between both. Saintillan and Shelley [43] derived a basic kinetic model for a suspension of self-propelled rodlike particles and discussed its stability and nonlinear dynamics. Weady *et al.* [44] restated and coarse grained a continuum kinetic model for an active suspension. These two models approximate the translational diffusion to a constant, while in fact, this diffusion is anisotropic and depends on the orientation of the particle. A macromodel that considers the coupling of concentration and orientation of Brownian rods is not yet available in the literature. This mutual coupling is especially interesting in the context of active nematic suspensions. Typical models of active nematic suspensions assume isotropic diffusion and therefore uniform concentration; however many physical systems show significant fluctuations [45].

This work aims to build a new macromodel to solve the motion of suspended rodlike particles in flows in a nonhomogeneous system taking into consideration the coupling of particle concentration and orientation. To verify this model, a new numerical strategy is developed to solve the configurational and spatial Fokker-Planck equation of suspension of Brownian particles in a Newtonian viscous fluid. Particle suspensions are studied in a planar channel and with the presence of a circular obstacle. The structure of this article is as follows. Section II focuses on the theoretical modeling.

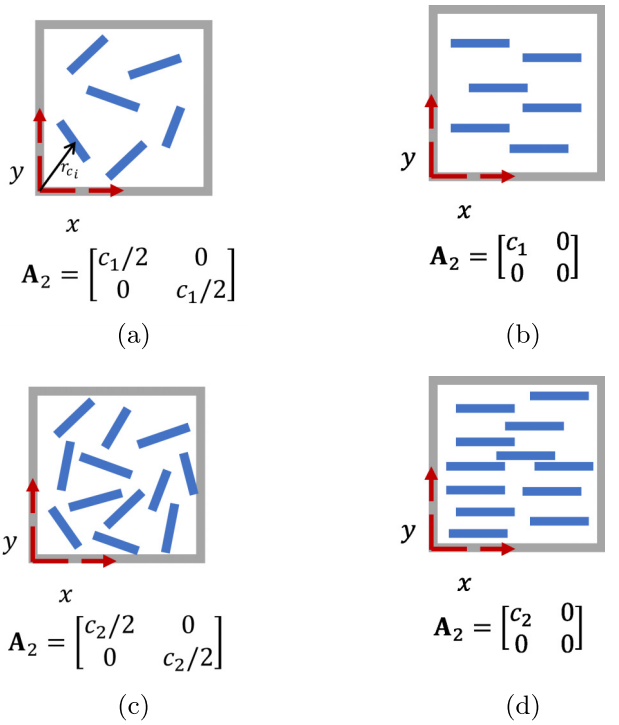

FIG. 1. Representation of $\mathbf{A}_2$ in an elementary surface for different concentrations and orientations. (a) Two-dimensional random rods with concentration c_1. (b) Perfectly aligned rods in the x direction with concentration c_1. (c) Two-dimensional random rods with concentration c_2. (d) Perfectly aligned rods in the x direction with concentration c_2.

Then Sec. III describes the flow problem used to solve the rodlike particle suspensions. Finally, before the conclusion, Sec. IV shows the numerical results in the two geometries, planar channel with and without a circular obstacle, and the verification of the macromodel.

II. THEORETICAL MODEL

A. Hypotheses

Let us consider a suspension of Brownian rodlike particles of length L and width D. The particles are monodisperse, neutrally buoyant, and rigid. The suspension is considered in the dilute regime of concentration, where $c \ll (D/L)^2$. Each particle is described with a position vector of the particle's centroid $\mathbf{r}_c$ and an orientation unit vector $\mathbf{p}$.

B. Kinetic model equation

A suspension of Brownian particles can be described via a probability distribution function $\Psi(\mathbf{r}_c, \mathbf{p}, t)$. It represents the probability to find a particle at location $\mathbf{r}_c$, at the level of elementary volume [see Fig. 1(a)], with orientation $\mathbf{p}$ at time t. In the dilute regime, a single-particle Smoluchowski equation can be obtained as follows [4,7,19,46]

$$\frac{\partial \Psi}{\partial t} = -\nabla_{\mathbf{x}} \cdot (\dot{\mathbf{r}}_c \Psi) - \nabla_{\mathbf{p}} \cdot (\dot{\mathbf{p}} \Psi). \tag{1}$$

The evolution of the position of a Brownian particle with respect to time, $\dot{\mathbf{r}}_c$, is

$$\dot{\mathbf{r}}_c = \mathbf{u} - \mathbf{D}_t \cdot \nabla_{\mathbf{x}} \log \Psi, \tag{2}$$

and the evolution of its orientation with respect to time, $\dot{\mathbf{p}}$, can be written as

$$\dot{\mathbf{p}} = \dot{\mathbf{p}}_j - D_r \nabla_{\mathbf{p}} \log \Psi, \tag{3}$$

where $\dot{\mathbf{p}}_j$ is the Jeffery's equation and it is given by

$$\dot{\mathbf{p}}_j = -\frac{1}{2}\boldsymbol{\omega} \cdot \mathbf{p} + \frac{\lambda}{2}(\dot{\boldsymbol{\gamma}} \cdot \mathbf{p} - \dot{\boldsymbol{\gamma}} : \mathbf{ppp}). \tag{4}$$

D_r and $\mathbf{D}_t$ are the rotary diffusion coefficient and translational diffusion tensor, respectively. The latter for nonspherical, rigid particles are defined by $\mathbf{D}_t = D_{\parallel}\mathbf{pp} + D_{\perp}(\boldsymbol{\delta} - \mathbf{pp})$, where $D_{\parallel}$ and $D_{\perp}$ are constants that characterize the diffusion parallel and perpendicular to the particle axis. The rotary diffusion can also have a tensorial form similar to $\mathbf{D}_t$. However, the scalar product of $\mathbf{p}$ with $\nabla_{\mathbf{p}}$ equals zero, which reduces the rotary diffusion to a scalar [19]. $\mathbf{u}$ is the external flow velocity vector at location $\mathbf{r}_c$. $\nabla_{\mathbf{p}}$ and $\nabla_{\mathbf{x}}$ denote the gradient operators in configurational and spatial spaces, respectively. $\boldsymbol{\omega}$, $\dot{\boldsymbol{\gamma}}$, and $\boldsymbol{\delta}$ are the vorticity, strain rate, and identity tensors, respectively. λ is a constant form factor as a function of the rod aspect ratio $a_r = L/D$. Hence, the expanded version of Eq. (1), by taking into account the fluid incompressibility condition, is

$$\frac{D\Psi}{Dt} = \nabla_{\mathbf{x}} \cdot (\mathbf{D}_t \cdot \nabla_{\mathbf{x}}\Psi) - \nabla_{\mathbf{p}} \cdot (\dot{\mathbf{p}}_j \Psi) + D_r \nabla_{\mathbf{p}}^2 \Psi, \tag{5}$$

where $\frac{D(\ldots)}{Dt} = \frac{\partial(\ldots)}{\partial t} + \mathbf{u} \cdot \nabla_{\mathbf{x}}(\ldots)$ is the material derivative operator and $\nabla_{\mathbf{p}}^2$ is the Laplacian operator in configurational domain. In what follows, we derive an equivalent evolution equation based on the second-order moment of Ψ.

C. Second-order moment of Ψ

The second-order moment of Ψ, $\mathbf{A}_2$, contains information on the local concentration and orientation of particles and is defined as

$$\mathbf{A}_2 = \frac{1}{V}\int_{\mathbf{p}}\int_{\mathbf{r}_c} \mathbf{pp}\Psi d\mathbf{r}_c d\mathbf{p}. \tag{6}$$

The trace of $\mathbf{A}_2$ is the concentration field c, which represents the mean number density in the suspension; it is the zeroth-order moment of Ψ,

$$c = \frac{1}{V}\int_{\mathbf{p}}\int_{\mathbf{r}_c} \Psi d\mathbf{r}_c d\mathbf{p}. \tag{7}$$

V represents the volume, which is large enough to contain a statistically significant number of particles but smaller than the characteristic length scale of the macroscopic properties of the system under consideration. Figure 1 provides two-dimensional (2D) examples on how $\mathbf{A}_2$ can describe the particle concentration and orientation in an elementary volume. It represents $\mathbf{A}_2$ for two concentrations c_1 and c_2, with $c_2 \geqslant c_1$. At the macroscopic level, $\mathbf{A}_2 = \mathbf{A}_2(\boldsymbol{x}, t)$, where $\mathbf{x}$ is the position vector of the elementry volume.

The evolution of $\mathbf{A}_2$ is obtained by premultiplying Eq. (5) with the tensor $\mathbf{pp}/V$ and integrating it over the spatial and configurational spaces. We focus here on the first term on the right-hand side of Eq. (5), since the material derivative of the orientational divergence part of Eq. (5) is similarly

derived in the literature [40]. First, the divergence operator is expanded to obtain

$$\frac{1}{V}\int_{\mathbf{p}}\int_{\mathbf{r}_c}\nabla_{\mathbf{x}}\cdot(\mathbf{D}_t\cdot\nabla_{\mathbf{x}}\Psi)\mathbf{p}\mathbf{p}d\mathbf{r}_c d\mathbf{p}=\frac{1}{V}\nabla_{\mathbf{x}}\cdot\nabla_{\mathbf{x}}\cdot\int_{\mathbf{p}}\int_{\mathbf{r}_c}\mathbf{D}_t\mathbf{p}\mathbf{p}\Psi d\mathbf{r}_c d\mathbf{p}$$
$$=D_\perp\nabla_{\mathbf{x}}^2\mathbf{A}_2+(D_\parallel-D_\perp)\nabla_{\mathbf{x}}\nabla_{\mathbf{x}}:\mathbf{A}_4, \tag{8}$$

where $\mathbf{A}_4=\frac{1}{V}\int_{\mathbf{p}}\int_{\mathbf{r}_c}\mathbf{pppp}\Psi d\mathbf{r}_c d\mathbf{p}$ is the fourth-order moment of Ψ. After the full derivation, the evolution of the tensor $\mathbf{A}_2$ is obtained,

$$\frac{D\mathbf{A}_2}{Dt}=-\frac{1}{2}(\boldsymbol{\omega}\cdot\mathbf{A}_2-\mathbf{A}_2\cdot\boldsymbol{\omega})+\frac{\lambda}{2}(\dot{\boldsymbol{\gamma}}\cdot\mathbf{A}_2+\mathbf{A}_2\cdot\dot{\boldsymbol{\gamma}}-2\mathbf{A}_4:\dot{\boldsymbol{\gamma}})$$
$$+2D_r(c\boldsymbol{\delta}-\alpha\mathbf{A}_2)+D_\perp\nabla_{\mathbf{x}}^2\mathbf{A}_2+(D_\parallel-D_\perp)\nabla_{\mathbf{x}}\nabla_{\mathbf{x}}:\mathbf{A}_4, \tag{9}$$

where α equals 2 in 2D and 3 in 3D. The full derivation of Eq. (9) is reported in Appendix A. It can be noticed that the time evolution of the tensor $\mathbf{A}_2$ depends on higher-order moments of Ψ. Hence, the problem requires a closure approximation. Fortunately, the standard closure approximations [47–49] can be applied for this case, where the particles are axisymmetric, by being careful to normalize the tensor $\mathbf{A}_2$ by c to maintain the condition of having a unitary trace. The Tucker and coworkers model is recovered from Eq. (9) by setting the translational diffusion to zero (i.e., $D_\perp = D_\parallel = 0$) and then dividing by the trace of $\mathbf{A}_2$ [40]. The last term in Eq. (9) is the Hessian operator and the last two terms of Eq. (9) show implicitly the coupling between the local concentration and the local orientation of Brownian particles. It is explained in Sec. II D. The last two terms have been omitted in recent works but they can change drastically the obtained microstructures as we will discuss below [41,44,50,51].

The derived macromodel enables one to solve a set of partial differential equations (PDEs) rather than a full 6D Fokker-Planck equation [Eq. (5)], to be discussed below, drastically simplifying the problem.

D. Concentration field of Brownian rods

The concentration field c is represented by the trace of $\mathbf{A}_2$. So the evolution of concentration of the Brownian rods in a suspending fluid can be derived from Eq. (9)

$$\frac{Dc}{Dt}=D_\perp\nabla_{\mathbf{x}}^2 c+(D_\parallel-D_\perp)\nabla_{\mathbf{x}}\nabla_{\mathbf{x}}:\mathbf{A}_2. \tag{10}$$

The last term in Eq. (10) (Hessian operator) shows the coupling between the concentration and the local orientation of the Brownian rods and it requires knowledge of $\mathbf{A}_2$, while $\mathbf{A}_2$ does not appear in the concentration equation when diffusion is isotropic (i.e., $D_\parallel = D_\perp$).

E. Dimensionless formulation of the problem

The problem identified by Eq. (5), or by Eq. (9) in its tensor form, describes the evolution of spatial and orientational configurations of a suspension of Brownian rodlike particles in a flow field. These systems of equations will be analyzed numerically in the following sections. Choosing the particle length L as the characteristic length and the characteristic strain rate $|\dot{\gamma}| = U_{\text{avg}}/L$, where U_{avg} is the average flow velocity, the definitions of the dimensionless variables for the problem,

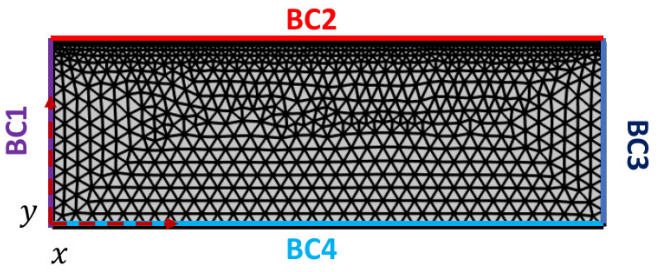

(a)

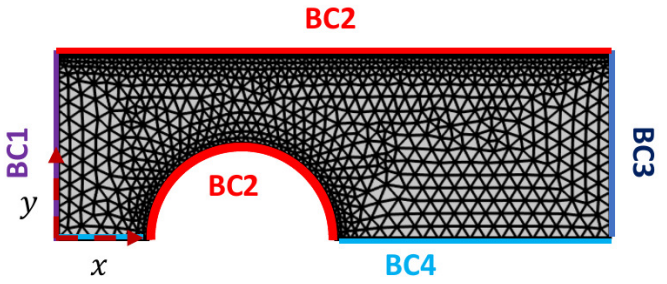

(b)

FIG. 2. FE mesh for a planar channel. BC1, laminar inflow; BC2, pressure outlet; BC3, zero-slip condition; and BC4, symmetry condition. (a) Rectangular planar channel. (b) Planar channel with circular obstacle.

denoted with an asterisk, are

$$t^* = t|\dot{\gamma}|, \tag{11}$$

$$\mathbf{u}^* = \frac{\mathbf{u}}{L|\dot{\gamma}|}, \tag{12}$$

$$\mathrm{Pe}_r = \frac{|\dot{\gamma}|}{D_r}, \tag{13}$$

$$\dot{\mathbf{p}}_\mathbf{j}^* = \frac{\dot{\mathbf{p}}_\mathbf{j}}{|\dot{\gamma}|}, \tag{14}$$

and

$$\mathbf{D}^* = \frac{\mathbf{D}_t}{L^2|\dot{\gamma}|} = \frac{1}{\mathrm{Pe}_\parallel}\mathbf{pp} + \frac{1}{\mathrm{Pe}_\perp}(\boldsymbol{\delta} - \mathbf{pp}). \tag{15}$$

The rotary Peclet number (Pe_r) appears, which measures the distortion of the suspension orientation state from the anisotropic equilibrium orientation configuration, i.e., changing Pe_r tends to affect the final orientation. It also shows the two translational Brownian Peclet numbers ($\mathrm{Pe}_\parallel = L^2|\dot{\gamma}|/D_\parallel$) and ($\mathrm{Pe}_\perp = L^2|\dot{\gamma}|/D_\perp$), along and orthogonal to the long axis of the rod, respectively.

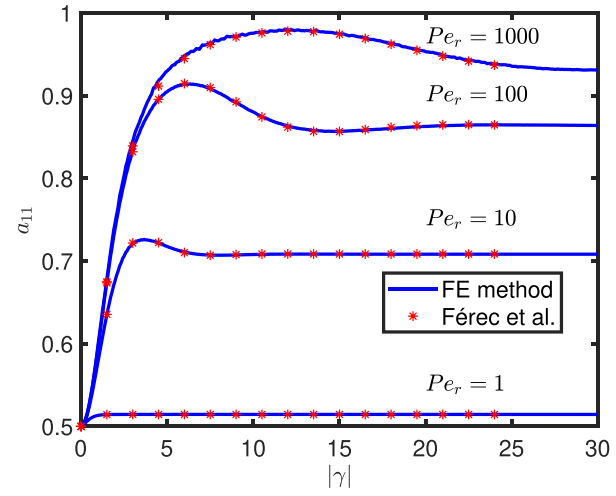

(a)

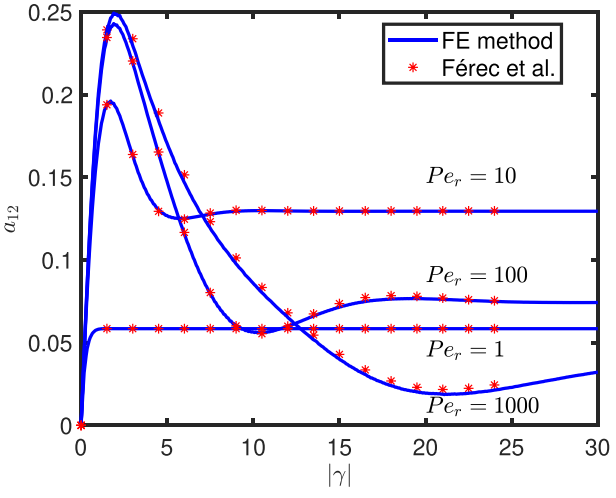

(b)

FIG. 3. a_{11} and a_{12} versus strain for the streamline along the line $y = 0.9H$ in a planar channel, with $|\dot{\gamma}| = 1.8/s$. Method 1 is verified with the work of Férec *et al.* [52]. (a) Evolution of orientation component a_{11} as a function of strain $|\gamma|$. (b) Evolution of orientation component a_{12} as a function of strain $|\gamma|$.

The dimensionless form of the Fokker-Planck equation becomes after dropping the asterisk

$$\frac{D\Psi}{Dt} = \nabla_{\mathbf{x}} \cdot \left\{ \left[\frac{1}{\mathrm{Pe}_{\parallel}} \mathbf{pp} + \frac{1}{\mathrm{Pe}_{\perp}} (\boldsymbol{\delta} - \mathbf{pp}) \right] \cdot \nabla_{\mathbf{x}} \Psi \right\} - \nabla_{\mathbf{p}} \cdot (\dot{\mathbf{p}}_j \Psi) + \frac{1}{\mathrm{Pe}_r} \nabla_{\mathbf{p}}^2 \Psi. \tag{16}$$

For very long and thin rodlike particles, the relation $\mathrm{Pe}_{\perp} = 2\mathrm{Pe}_{\parallel}$ applies [19], and Eq. (15) simplifies as $\mathbf{D} = \frac{1}{\mathrm{Pe}_{\perp}} (\mathbf{pp} + \boldsymbol{\delta})$ and $\lambda = 1$. Equation (16) is written as

$$\frac{D\Psi}{Dt} = \nabla_{\mathbf{x}} \cdot \left\{ \left[\frac{1}{\mathrm{Pe}_{\perp}} (\mathbf{pp} + \boldsymbol{\delta}) \right] \cdot \nabla_{\mathbf{x}} \Psi \right\} - \nabla_{\mathbf{p}} \cdot (\dot{\mathbf{p}}_j \Psi) + \frac{1}{\mathrm{Pe}_r} \nabla_{\mathbf{p}}^2 \Psi. \tag{17}$$

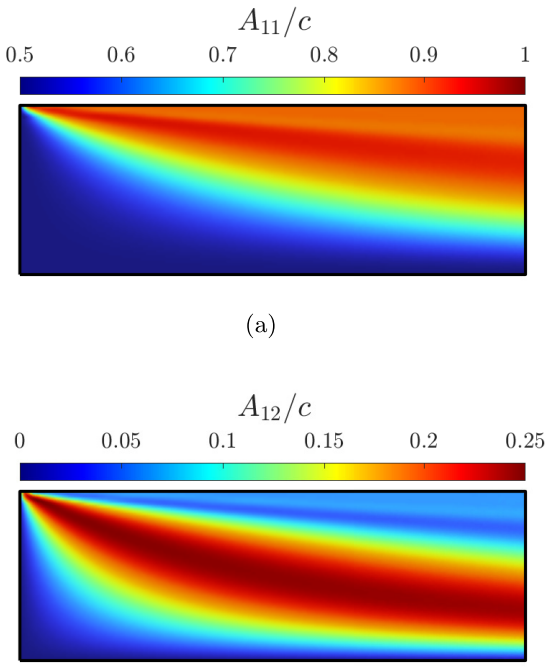

FIG. 4. (a) A_{11}/c and (b) A_{12}/c components of the orientation tensor, $\mathbf{A}_2$, along the channel in a homogeneous system, where concentration equals 1 at the inlet and no rod migrations occur. (a) Distribution of the orientation component A_{11}/c in the xy plane of a planar channel. (b) Distribution of the orientation component A_{12}/c in the xy plane of a planar channel.

Using the same dimensionless variables, the evolution equation for the second-order moment of the probability distribution function in dimensionless form is

$$\frac{D\mathbf{A}_2}{Dt} = -\frac{1}{2}(\boldsymbol{\omega}\cdot\mathbf{A}_2 - \mathbf{A}_2\cdot\boldsymbol{\omega}) + \frac{1}{2}(\dot{\boldsymbol{\gamma}}\cdot\mathbf{A}_2 + \mathbf{A}_2\cdot\dot{\boldsymbol{\gamma}} - 2\dot{\boldsymbol{\gamma}}:\mathbf{A}_4) + \frac{2}{\mathrm{Pe}_r}(c\boldsymbol{\delta} - \alpha\mathbf{A}_2) + \frac{1}{\mathrm{Pe}_\perp}\nabla^2_{\mathbf{x}}\mathbf{A}_2 + \frac{1}{\mathrm{Pe}_\perp}\nabla_{\mathbf{x}}\nabla_{\mathbf{x}}:\mathbf{A}_4. \tag{18}$$

III. FLOW PROBLEM

Under the assumptions of a Newtonian, isothermal, steady, and incompressible fluid, the governing equations for the pressure, P, and velocity fields in the dimensionless form are

$$\nabla_{\mathbf{x}}\cdot\mathbf{u} = 0, \tag{19}$$

$$\nabla^2_{\mathbf{x}}\mathbf{u} - \nabla_{\mathbf{x}}P = \mathbf{0}. \tag{20}$$

For simplicity, we do not consider here the coupling between flow and the extra stresses induced by rods since the goal is first to verify the obtained macromodel predictions and compare them with the full numerical solution of Eq. (16). This coupling will be explored in future works. This

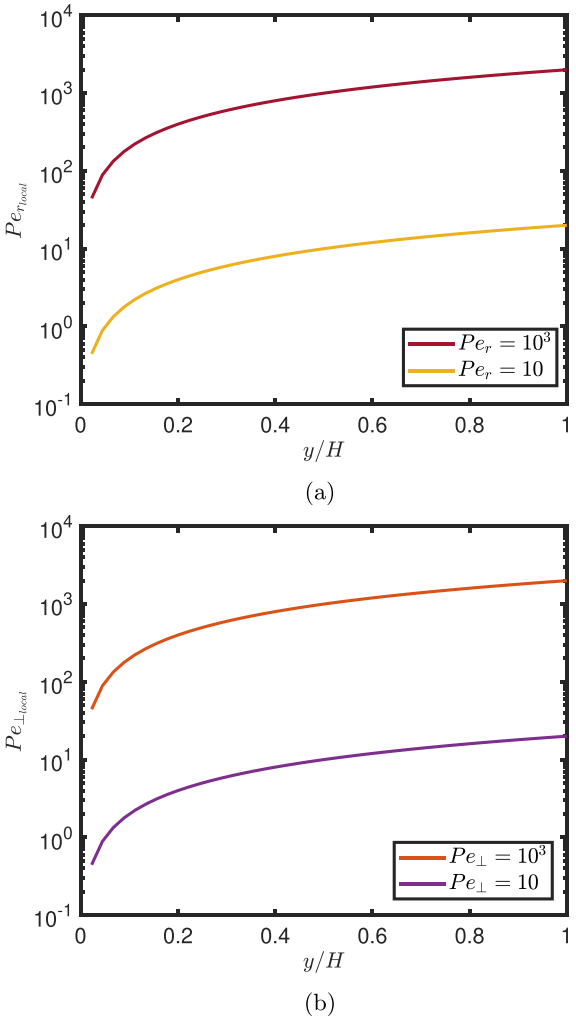

FIG. 5. Variation of local Peclet numbers with respect to the normalized channel width in a planar channel for the global Peclet numbers $\mathrm{Pe}_\perp = 10, 10^3$ and $\mathrm{Pe}_r = 10, 10^3$. (a) Evolution of the local rotary Peclet number, $\mathrm{Pe}_{r_{\mathrm{local}}}$, with respect to the normalized channel width, y/H, independent on the translational Peclet number. (b) Evolution of the local translational Peclet number, $\mathrm{Pe}_{\perp_{\mathrm{local}}}$, with respect to the normalized channel width y/H independent on the rotary Peclet number.

hypothesis is acceptable here in the assumption of dilute concentration regimes. Hence the problem is fully characterized by two Peclet numbers, Pe_r and $\mathrm{Pe}_\perp$.

The work is performed in a planar channel [Fig. 2(a)] of width $2H$ and length $W = 3H$, except for the case of the homogeneous inlet in a planar channel (Sec. IV B 1), where $W = 9H$. These dimensions do not affect our conclusions. $H = 1$ and is considered to be very large comparable to L ($H \gg L$). In the second part of the work, a circular obstacle of radius $R = 0.5H$ is introduced [Fig. 1(b)], the center of the obstacle is at $x = H$. Four types of boundary conditions, marked by BC1 to BC4, are defined for this model. BC1 is the inlet velocity profile condition $U/U_{\max} = 1 - (y/H)^2$ and the Dirichlet boundary conditions for Ψ; BC2 is the no slip condition at walls ($\mathbf{u} = \mathbf{0}$); BC3 is the outlet condition where the relative pressure is set to zero, $(-P\boldsymbol{\delta} + \nabla_{\mathbf{x}}\mathbf{u}) : \mathbf{nn} = 0$, where $\mathbf{n}$ is the normal vector to the surface; and BC4 is the symmetry boundary condition ($\mathbf{u} \cdot \mathbf{n} =$

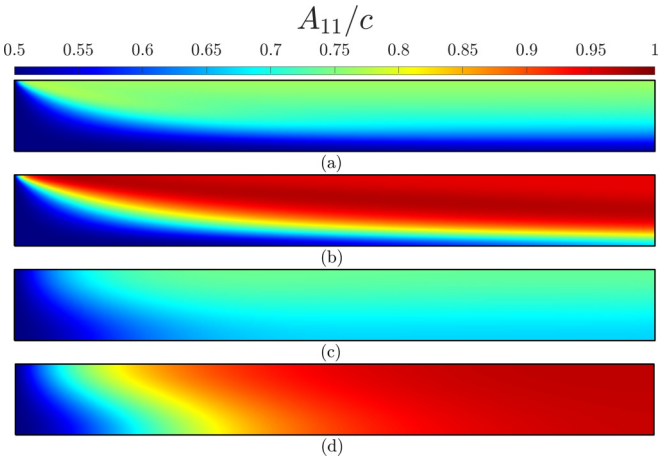

FIG. 6. Orientation component A_{11}/c using method 1, across the planar channel, where homogeneous concentration and random orientation of the rods are prescribed at the inlet for (a) $\mathrm{Pe}_r = 10, \mathrm{Pe}_\perp = 10^3$; (b) $\mathrm{Pe}_r = 10^3, \mathrm{Pe}_\perp = 10^3$; (c) $\mathrm{Pe}_r = 10, \mathrm{Pe}_\perp = 10$; and (d) $\mathrm{Pe}_r = 10^3, \mathrm{Pe}_\perp = 10$.

0 and $\dot{\boldsymbol{\gamma}} - (\dot{\boldsymbol{\gamma}} \cdot \mathbf{n})\mathbf{n} = \mathbf{0}$). Due to BC4, half of the domain is considered in simulations to reduce computational efforts (see Fig. 2). The homogeneous Neumann boundary conditions (zero flux) is applied for the probability density function Ψ in method 1 ($\mathbf{n} \cdot \nabla_{\mathbf{x}} \Psi = 0$ for spatial BCs (BC2, BC3, and BC4) and $\mathbf{n} \cdot \nabla_{\mathbf{p}} \Psi = 0$ for configurational BCs [all the surfaces in Fig. 21(b) except BC5)]. It is also used for $\mathbf{A}_2$ and c in method 2 ($\mathbf{n} \cdot \nabla_{\mathbf{x}} A_{ij} = 0$, where A_{ij} are the components of $\mathbf{A}_2$ and $\mathbf{n} \cdot \nabla_{\mathbf{x}} c = 0$).

IV. NUMERICAL RESULTS

The steady-state form of Eq. (17) is

$$\mathbf{u} \cdot \nabla_{\mathbf{x}} \Psi = \nabla_{\mathbf{x}} \cdot \left\{ \left[\frac{1}{\mathrm{Pe}_\perp} (\mathbf{pp} + \boldsymbol{\delta}) \right] \cdot \nabla_{\mathbf{x}} \Psi \right\} - \nabla_{\mathbf{p}} \cdot (\dot{\mathbf{p}}_j \Psi) + \frac{1}{\mathrm{Pe}_r} \nabla_{\mathbf{p}}^2 \Psi, \tag{21}$$

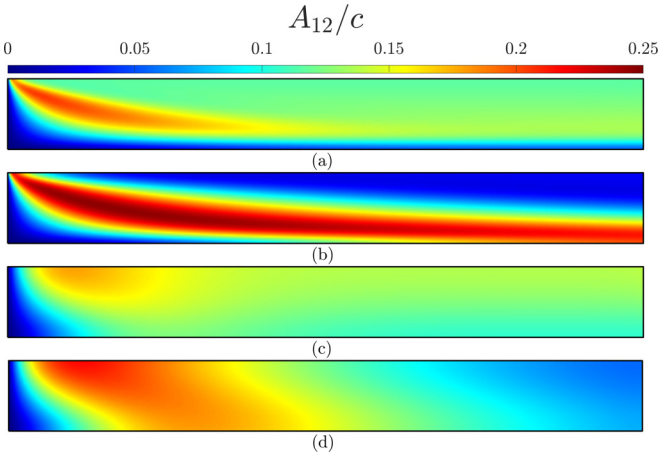

FIG. 7. Orientation component A_{12}/c using method 1, across the planar channel, where homogeneous concentration and random orientation of the rods are prescribed at the inlet for (a) $\mathrm{Pe}_r = 10, \mathrm{Pe}_\perp = 10^3$; (b) $\mathrm{Pe}_r = 10^3, \mathrm{Pe}_\perp = 10^3$; (c) $\mathrm{Pe}_r = 10, \mathrm{Pe}_\perp = 10$; and (d) $\mathrm{Pe}_r = 10^3, \mathrm{Pe}_\perp = 10$.

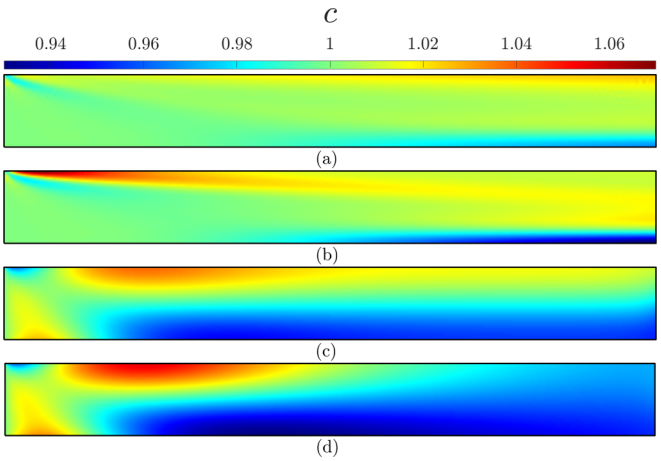

FIG. 8. Concentration distribution c using method 1, across the planar channel, where homogeneous concentration and random orientation of the rods are prescribed at the inlet for (a) $\mathrm{Pe}_r = 10, \mathrm{Pe}_\perp = 10^3$; (b) $\mathrm{Pe}_r = 10^3, \mathrm{Pe}_\perp = 10^3$; (c) $\mathrm{Pe}_r = 10, \mathrm{Pe}_\perp = 10$; and (d) $\mathrm{Pe}_r = 10^3, \mathrm{Pe}_\perp = 10$.

and of Eq. (18) is

$$\mathbf{u}\cdot\nabla_{\mathbf{x}}\mathbf{A}_2 = -\frac{1}{2}(\boldsymbol{\omega}\cdot\mathbf{A}_2 - \mathbf{A}_2\cdot\boldsymbol{\omega}) + \frac{1}{2}(\dot{\boldsymbol{\gamma}}\cdot\mathbf{A}_2 + \mathbf{A}_2\cdot\dot{\boldsymbol{\gamma}} - 2\dot{\boldsymbol{\gamma}}:\mathbf{A}_4) + \frac{2}{\mathrm{Pe}_r}(c\boldsymbol{\delta} - \alpha\mathbf{A}_2) + \frac{1}{\mathrm{Pe}_\perp}\nabla_{\mathbf{x}}^2\mathbf{A}_2 + \frac{1}{\mathrm{Pe}_\perp}\nabla_{\mathbf{x}}\nabla_{\mathbf{x}}:\mathbf{A}_4. \tag{22}$$

Equations (19), (20), and (21) and Eqs. (19), (20), and (22) are solved numerically using method 1 and method 2, respectively (see Appendix B). Both methods use the finite-element method (FEM). The numerical solutions are tested at steady state and for 2D flows to reduce computational time. Method 1 is based on the linear extrusion of 2D flow channel, represents the spatial distribution in

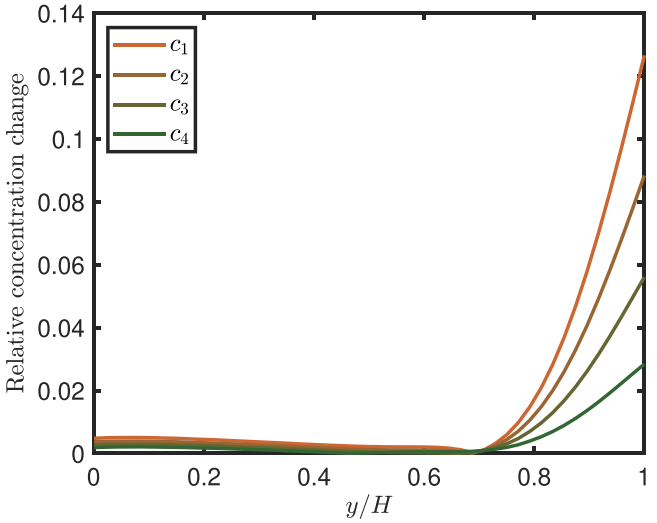

FIG. 9. Relative change in concentration with respect to the normalized channel width, y/H, at the outlet, for $\mathrm{Pe}_r = 10^3$ and $\mathrm{Pe}_\perp = 10$, for the four concentration gradients c_1, c_2, c_3, and c_4.

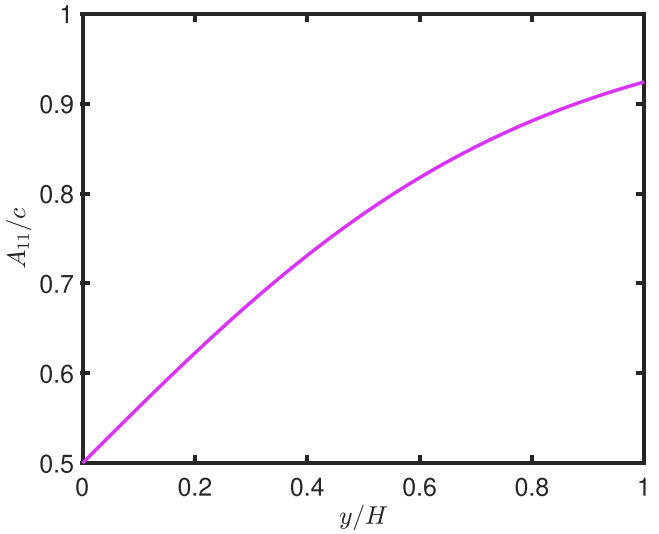

FIG. 10. Orientation component A_{11}/c with respect to the normalized channel width, y/H, at the inlet.

xy plane, to a third dimension, which stands for the probability of finding a rod of orientation angle with the x axis ϕ. Method 2 is based on solving the set of equations of evolution of A_{11}, A_{12}, and A_{22} in the flow.

A. Method 1 verification

1. Homogeneous systems

To verify the numerical solution of the model, we compare the model with published data in the case of an homogeneous system [33,52]. The flow field is assumed to be at steady state. In this case, the streamlines are parallel to each other and parallel to the wall. No Brownian translational diffusion is taken into consideration. The flow inside the channel is described as a planar Poiseuille flow in the direction of x. These assumptions allow us to study the rod orientations in the flow channel, since the shear rate in the Poiseuille flow is constant along each streamline. Rods are assumed to have a random-planar distribution of homogeneous concentration at the inlet, which means a Dirichlet boundary condition of $\Psi = 1/2\pi$.

To verify the results of the FEM in a homogeneous system, rod orientations at a chosen streamline is compared with the results found in the literature (see Fig. 3). Equation (21) is solved using a homogenous numerical diffusion to stabilize the numerical scheme, which gives

$$\mathbf{u} \cdot \nabla_{\mathbf{x}} \Psi = \frac{1}{\mathrm{Pe}_{\mathrm{num}}} \nabla_{\mathbf{x}}^2 \Psi - \nabla_{\mathbf{p}} \cdot (\dot{\mathbf{p}}_j \Psi) + \frac{1}{\mathrm{Pe}_r} \nabla_{\mathbf{p}}^2 \Psi. \tag{23}$$

$\mathrm{Pe}_{\mathrm{num}}$ is an artificial diffusion Peclet number, set to value 10^9, which has no physical effect except for stabilizing the numerical scheme. The study is done for values of rotary Peclet number Pe_r= 1, 10, 100, and 1000. The orientation state of the rods is represented by the components of the second-order orientation tensor $\mathbf{a}_2$ ($\mathbf{a}_2 = \int_{\mathbf{p}} \mathbf{pp}\psi d\mathbf{p}$, where ψ is the probability distribution function of finding a rod of orientation $\mathbf{p}$ at time t in a homogeneous systems [40]) (see Fig. 3). In addition, these quantities are traced spatially along the channel for $\mathrm{Pe}_r = 100$ and compared with the results in the literature (Fig. 4).

The a_{11} and a_{12} components are directly computed from the FP equation for planar orientations and compared with the results obtained by Férec *et al.* [52] solving the configurational part of Eq. (5) with a finite-volume method approach. Figure 3 shows the very good agreement between the two

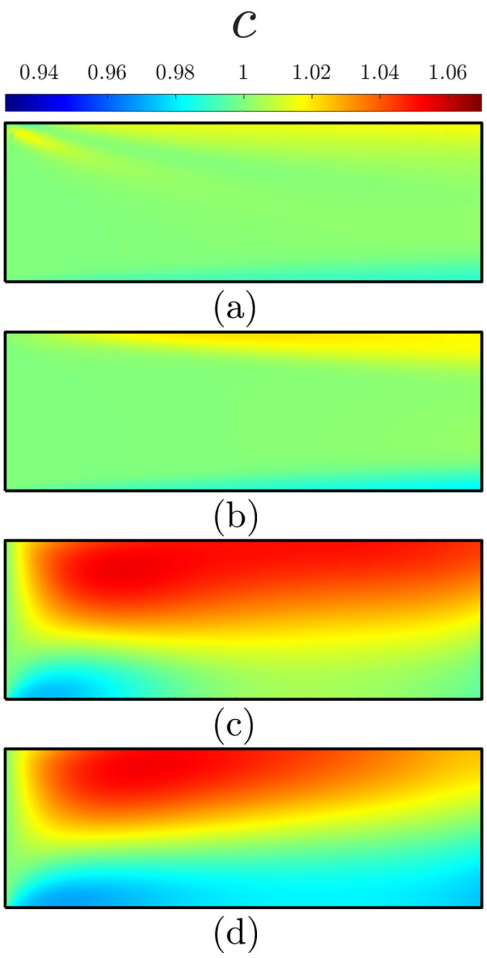

FIG. 11. Concentration distribution c using method 1, across the planar channel, where homogeneous concentration and aligned rods at the inlet for (a) $\mathrm{Pe}_r = 10$, $\mathrm{Pe}_\perp = 10^3$; (b) $\mathrm{Pe}_r = 10^3$, $\mathrm{Pe}_\perp = 10^3$; (c) $\mathrm{Pe}_r = 10$, $\mathrm{Pe}_\perp = 10$; and (d) $\mathrm{Pe}_r = 10^3$, $\mathrm{Pe}_\perp = 10$.

methods. Figure 4 shows that rods along the fixed wall become highly oriented and reach its final orientation almost instantly, whereas rods further downstream must travel quite a distance to reach the steady state. These results (Fig. 4) show agreement with the work done by Mezi *et al.* [33], where we get $\mathbf{A}_2/c = \mathbf{a}_2$.

2. Nonhomogeneous systems

A concentration gradient is imposed at the inlet along the y axis. The Dirichlet boundary condition is set to be $\Psi = \frac{c_0}{2\pi}$, where $c_0 = 1 - 0.6(y/H)^2$ is the concentration at the inlet. This parabolic concentration gradient is chosen to have a nonzero concentration in the domain ($c_0 = 0.4$ at the walls and $c_0 = 1$ at the center). Rod orientations are planar random at the inlet and no Brownian translational diffusion is considered. BC1, BC2, BC3, and BC4 are taken into account. In these conditions, the rods are affected by pure translational convection of the flow, and no rod migration across the streamlines is expected. The effect of concentration gradients on rod orientation distribution is a major concern. A_{11}/c and A_{12}/c components are directly computed from the FP equation in the channel for $\mathrm{Pe}_r = 1$, 10, 100, and 1000. The results are similar to the previous part when homogeneous concentration along the channel is examined (see Figs. 3 and 4).

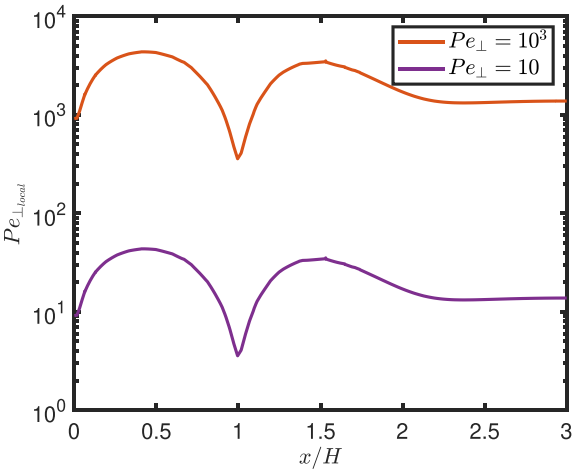

(a)

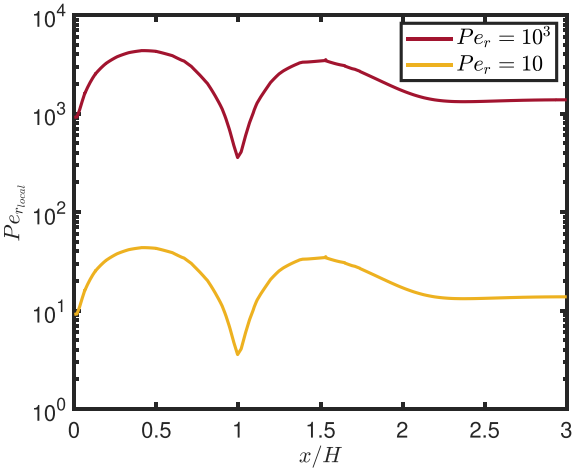

(b)

FIG. 12. Variation of local Peclet numbers with respect to the normalized channel width at the streamline $y = 0.7H$ in a planar channel with the presence of circular obstacle. (a) Evolution of the local rotary Peclet number, $\mathrm{Pe}_{r_{\mathrm{local}}}$, with respect to the normalized channel length, x/H, independent on the translational Peclet number. (b) Evolution of the local translational Peclet number, $\mathrm{Pe}_{\perp_{\mathrm{local}}}$, with respect to the normalized channel length x/H independent on the rotary Peclet number.

B. Effect of translational diffusion

We aim now to study the effect of the anisotropic translational diffusion on rod suspensions in a planar channel. Equations (19), (20), and (21) are solved based on method 1. Three regimes of translational and orientational diffusions are studied. The first regime, $\mathrm{Pe}_\perp \ll \mathrm{Pe}_r$, explores the case when the timescale for translational diffusion is longer than the rotational diffusion one. The second regime, $\mathrm{Pe}_\perp = \mathrm{Pe}_r$, considers the case where both timescales are equal, and the third regime, $\mathrm{Pe}_\perp \gg \mathrm{Pe}_r$, investigates the case where the rotary diffusion is faster than the translational diffusion. A local rotary, perpendicular, and parallel Peclet numbers are introduced depending on the local strain rate, $\dot{\gamma}_l = \sqrt{\frac{1}{2}(\dot{\boldsymbol{\gamma}} : \dot{\boldsymbol{\gamma}})}$, $\mathrm{Pe}_{r_{\mathrm{local}}} = |\dot{\gamma}_l|/D_r$, $\mathrm{Pe}_{\perp_{\mathrm{local}}} = (|\dot{\gamma}_l|H^2)/D_\perp$, and $2\mathrm{Pe}_{\parallel_{\mathrm{local}}} = \mathrm{Pe}_{\perp_{\mathrm{local}}}$, respectively. In a planar channel, the local Peclet numbers are constant along the flow direction (x axis). The variation

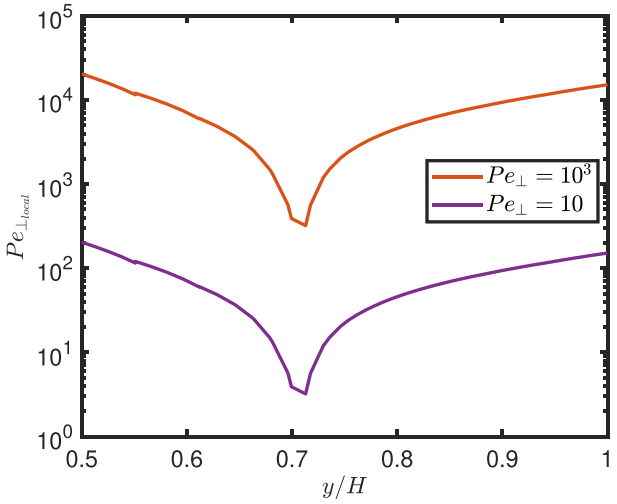

(a)

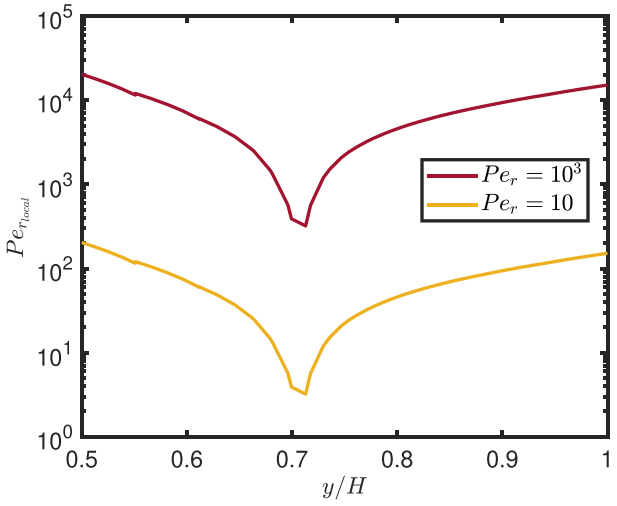

(b)

FIG. 13. Variation of local Peclet numbers with respect to the normalized channel length at $x = H$ in a planar channel with the presence of circular obstacle. (a) Evolution of the local rotary Peclet number, $\mathrm{Pe}_{r_{\mathrm{local}}}$, with respect to the normalized channel width, y/H, independent on the translational Peclet number. (b) Evolution of the local translational Peclet number, $\mathrm{Pe}_{\perp_{\mathrm{local}}}$, with respect to the normalized channel width, y/H, independent on the rotary Peclet number.

of local rotational and perpendicular Peclet numbers along the y axis are shown in Figs. 5(a) and 5(b). The rod suspensions are affected by the global and local Peclet numbers.

1. Homogeneous concentration and planar random orientation at the inlet

The rod concentration and orientation predictions are examined for a Dirichlet boundary condition $\Psi = 1/2\pi$. Figures 6 and 7 show that Brownian rods exhibit an inhomogeneous orientation through the channel. This is because of the competition between shear flow, which tends to align the rods in the flow direction, and Brownian motion, which tends to randomize their orientations

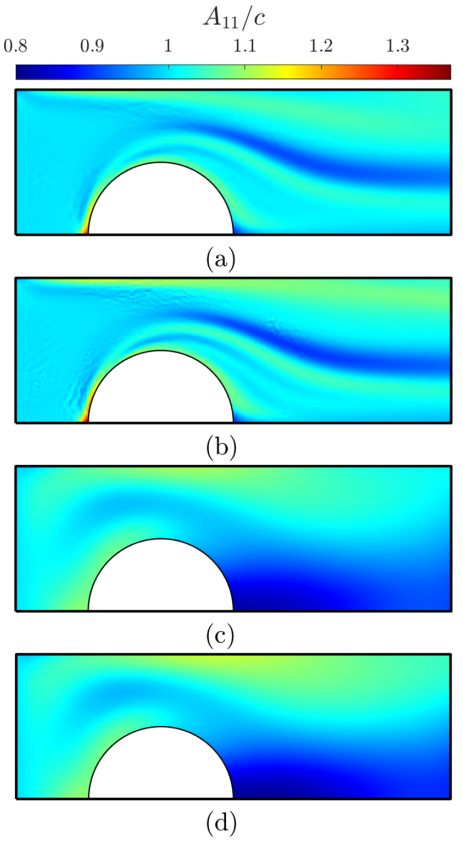

FIG. 14. Concentration distribution c using method 1, across the planar channel with the presence of circular obstacle, where homogeneous concentration and random orientation of the rods are prescribed at the inlet for (a) $\mathrm{Pe}_r = 10, \mathrm{Pe}_\perp = 10^3$; (b) $\mathrm{Pe}_r = 10^3, \mathrm{Pe}_\perp = 10^3$; (c) $\mathrm{Pe}_r = 10, \mathrm{Pe}_\perp = 10$; and (d) $\mathrm{Pe}_r = 10^3, \mathrm{Pe}_\perp = 10$.

[6,23,53]. The overshoot in the rod orientations before reaching the final orientation (see Fig. 3) is noticed in the channel. Depending on the rotary Peclet number, rods near the wall reaches their final orientation faster than the rods at the center due to the higher value of $\mathrm{Pe}_{r_{\mathrm{local}}}$ near the wall. For all the studied cases, A_{12}/c range between 0 and 0.25, which means that the angle between the rod and x axis ranges from 0 to $\frac{\pi}{2}$. Figure 8 shows that rods tend to migrate toward the walls, where $\mathrm{Pe}_{\perp_{\mathrm{local}}}$ is high.

This phenomenon was also predicted by Schiek and Shaqfeh [36] and by Nitsche and Hinch [37]. In Fig. 8(a) (where the high translational Peclet number, $\mathrm{Pe}_\perp = 10^3$, and low rotary Peclet number, $\mathrm{Pe}_r = 10$, are considered), rods migrate toward the wall. While in Fig. 8(b) (where the high translational Peclet number, $\mathrm{Pe}_\perp = 10^3$, and high rotary Peclet number, $\mathrm{Pe}_r = 10^3$, are considered) a high concentration is observed at the wall after the inlet. After a distance, rods accumulate between the center and the wall ($0.3 \leqslant y/H \leqslant 0.8$). This accumulation is due to the overshoot in rod orientations. Rods higher alignment leads to low migrations across the streamlines. At lower $\mathrm{Pe}_\perp$, rod migration is more evident. In Fig. 8(c), rod migration occurs and a concentration gradient is observed at the outlet. In this case, rods are less aligned, mainly in the center, which enhances rod migration toward the wall (higher local Peclet numbers). For the case of low translational Peclet number and high rotational Peclet number ($\mathrm{Pe}_\perp = 10$ and $\mathrm{Pe}_r = 10^3$), rods are highly aligned at the outlet and almost homogeneous [Fig. 6(d)]. Since the rod orientations tend to equilibrate

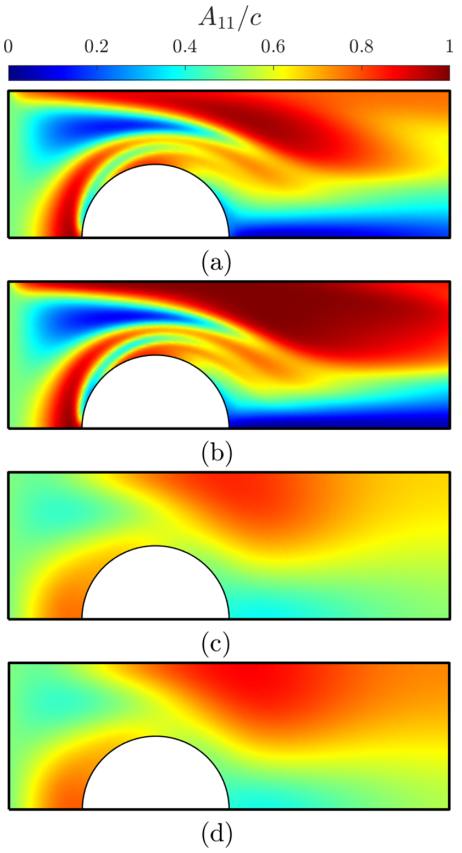

FIG. 15. Orientation component A_{11}/c using method 1, across the planar channel with the presence of circular obstacle, where homogeneous concentration and random orientation of the rods are prescribed at the inlet for (a) $\mathrm{Pe}_r = 10, \mathrm{Pe}_\perp = 10^3$; (b) $\mathrm{Pe}_r = 10^3, \mathrm{Pe}_\perp = 10^3$; (c) $\mathrm{Pe}_r = 10, \mathrm{Pe}_\perp = 10$; and (d) $\mathrm{Pe}_r = 10^3, \mathrm{Pe}_\perp = 10$.

significantly at lower strain than their center of mass translate in the flow direction. While the values of A_{11}/c is low near the wall [comparing with Fig. 6(b)] due to the migration of less aligned rods toward the wall.

2. Effect of concentration gradient at the inlet

A concentration gradient is introduced with a planar random orientation at the inlet $\Psi = c_i/(2\pi)$ to study its effect on the final rod suspension microstructures. Four different parabolic concentration profiles at the inlet are tested according to $c_i = -\frac{10-2i}{10}(y/H)^2 + 1$ for $i = 1, 2, 3$, and 4. Same effect of translational and rotational Peclet numbers is figured qualitatively as the previous section (Sec. IV B 1). No notable effect of concentration gradient on the orientation is shown. Rods are oriented similar to the case where homogeneous concentration is applied at the inlet (same plots for A_{11}/c and A_{12}/c in Figs. 6 and 7). This agrees with the results in Sec. IV A 2. However, concentration gradient at the inlet has a significant effect on rod migration rates. The relative changes in concentration $(\frac{|c-c_i|}{\mathrm{average}(c_i)})$ are plotted at the outlet for $\mathrm{Pe}_\perp = 10$ and $\mathrm{Pe}_r = 10^3$ in Fig. 9. Figure 9 shows that rod migrations are higher near the wall, where the concentration is the lowest for the four cases explored, and the gradient of local translational Peclet number is the highest. As concentration

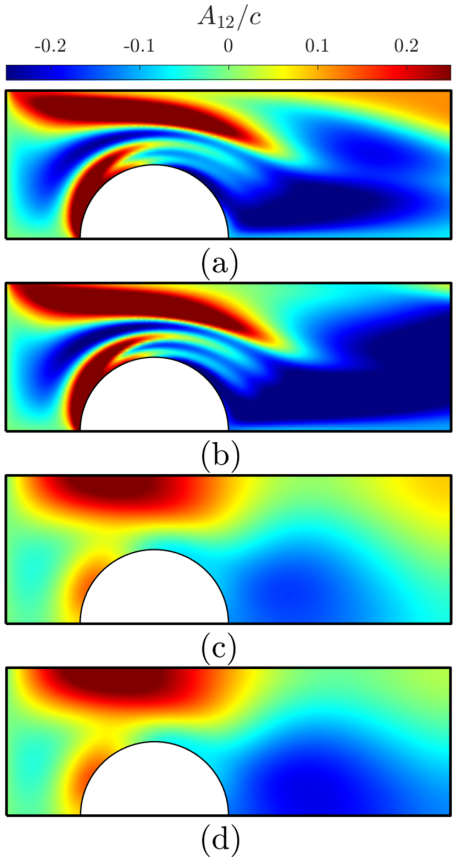

FIG. 16. Orientation component A_{12}/c orientation component using method 1, across the planar channel with the presence of circular obstacle, where homogeneous concentration and random orientation of the rods are prescribed at the inlet for (a) $\mathrm{Pe}_r = 10$, $\mathrm{Pe}_\perp = 10^3$; (b) $\mathrm{Pe}_r = 10^3$, $\mathrm{Pe}_\perp = 10^3$; (c) $\mathrm{Pe}_r = 10$, $\mathrm{Pe}_\perp = 10$; and (d) $\mathrm{Pe}_r = 10^3$, $\mathrm{Pe}_\perp = 10$.

gradient increases, rods migrate at higher rates due to rod migration from low to high translational $\mathrm{Pe}_{\perp_{\mathrm{local}}}$ regions.

C. Effect of rod orientations gradient at the inlet

To study the effect of rod orientations on its migration across streamlines, an orientation gradient is introduced at the inlet, where the Dirichlet boundary condition is $\Psi = [\frac{1}{2\pi}(e^{\beta}\ \sin^2\phi + e^{-\beta}\cos^2\phi)^{-1}]/2$, and $\beta = \frac{5y}{2H}$, where rods are planar random at the center of the channel and highly aligned in the direction of the flow near the walls (see Fig. 10 for A_{11}, and $A_{12} = 0$). The concentration is homogeneous and equals one at the inlet. Figure 11 shows that rods migrate toward the wall, where higher $\mathrm{Pe}_{\perp_{\mathrm{local}}}$. Comparing with the case of homogeneous concentration and planar random orientation at the inlet (Sec. IV B), the concentration at the center is almost the same, while near the wall, rods are more accumulated in the case of planar random at the inlet (comparing the case $\mathrm{Pe}_r = 10^3$, $\mathrm{Pe}_\perp = 10^3$ directly after the inlet). $c = 1.02$ where rods are perfectly aligned [Fig. 11(b)] and $c = 1.06$ where rods are planar random [Fig. 8(b)]. For lower translational Peclet number, $\mathrm{Pe}_\perp = 10$, rods are accumulated at the upper part [Figs. 11(c) and 11(d)]. In this zone, the migration of aligned particles is difficult. Qualitatively, the effect of orientation gradient at

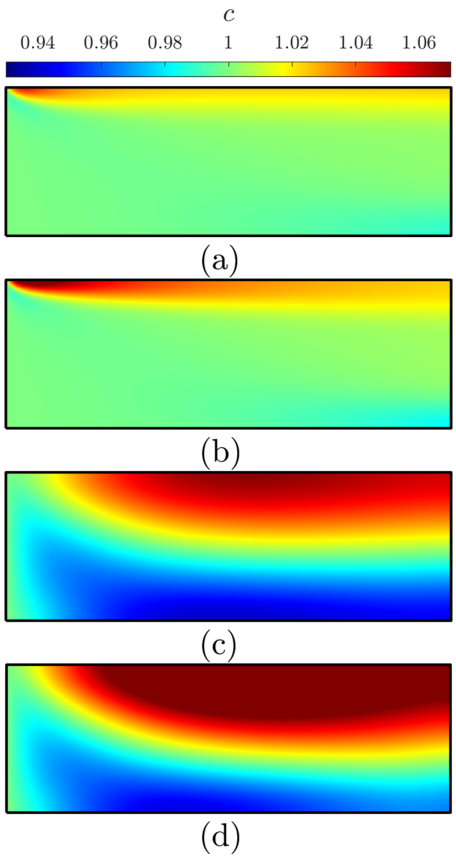

FIG. 17. Concentration distribution c results using a quadratic closure approximation, across the planar channel, where homogeneous concentration and random orientation of the rods are prescribed at the inlet for (a) $\mathrm{Pe}_r = 10$, $\mathrm{Pe}_\perp = 10^3$; (b) $\mathrm{Pe}_r = 10^3$, $\mathrm{Pe}_\perp = 10^3$; (c) $\mathrm{Pe}_r = 10$, $\mathrm{Pe}_\perp = 10$; and (d) $\mathrm{Pe}_r = 10^3$, $\mathrm{Pe}_\perp = 10$.

the inlet with the presence of the circular obstacle is similar to its effect in the absence of the obstacle.

D. Results of flow in a channel with a circular obstacle

Modeling the interaction between suspended rods and obstacles encountered in their flow is critical for understanding particulate suspension transport in various engineering applications [54,55]. A complex flow field is also interesting to explore here because of the expected variation of both local Peclet numbers along and perpendicular to the flow direction. Figure 12 depicts the variation of local Peclet numbers along a horizontal line at $y = 0.7H$. It shows that the local Peclet numbers have minima above the center ($x = H$) of the obstacle and maxima around the level of the extremities of the obstacle ($x = 0.5H$ and $x = 1.5H$). Figure 13 shows the variation of local Peclet numbers along a vertical line $x = H$. It shows that the local Peclet numbers have maxima near the wall and the obstacle, where the highest shear rate is found. Simulations are performed to study the effect of circular obstacles in the channel on the concentration and orientation.

In the presence of circular obstacle, rods are highly concentrated at the back of the obstacles and depleted in the front [56] as seen in Fig. 14. Even in the presence of the obstacle, rods have higher tendency to migrate toward the wall. Rods are more aligned at the back of the obstacle, as in Fig. 15 than at the front. This was also found by Phan-Thien and Graham [57], who used a single falling

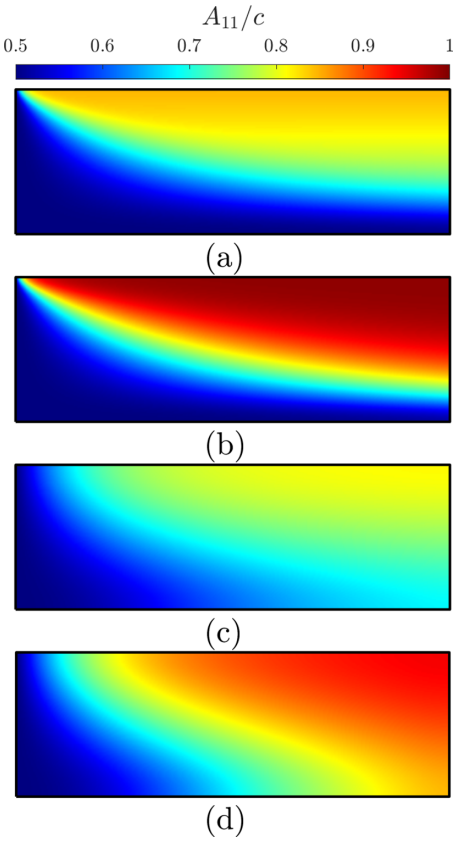

FIG. 18. Orientation component A_{11}/c results using a quadratic closure approximation, across the planar channel, where homogeneous concentration and random orientation of the rods are prescribed at the inlet for (a) $\mathrm{Pe}_r = 10$, $\mathrm{Pe}_\perp = 10^3$; (b) $\mathrm{Pe}_r = 10^3$, $\mathrm{Pe}_\perp = 10^3$; (c) $\mathrm{Pe}_r = 10$, $\mathrm{Pe}_\perp = 10$; and (d) $\mathrm{Pe}_r = 10^3$, $\mathrm{Pe}_\perp = 10$.

sphere in semiconcentrated systems, and by Kumar and Natale [58], who studied at low Reynolds values, two settling non-Brownian rigid spheres in a dilute suspension of Brownian rods. At the front of the obstacle, we find that the local orientation of the rods are aligned in the y direction ($A_{11}/c \leqslant 0.5$, and $A_{12}/c \leqslant 0$), as in Figs. 15 and 16. This is caused by the high shear rate zone, located above the obstacle. There, rods are less concentrated and less aligned because lower local Peclet numbers (see Fig. 13). Also, we see that rods have high alignment near the wall, even in the presence of circular obstacle due to the high local rotational Peclet numbers.

E. Macromodel

Although solving the Fokker-Planck equation is precise and general, it requires high computational effort. The second-moment tensor evolution [Eq. (22)] provides a concise description requiring less computational power. It is necessary to utilize a closure approximation to relate the fourth-order moment tensor with the second-order moment tensor to solve Eq. (22). Closure approximations found in the literature can be applied for this model. The numerical method 2 mentioned in Appendix B is used to solve Eq. (22), using quadratic [47] and IBOF [49] closures. We applied the quadratic closure for its simplicity, while the IBOF for its precision. This macromodel is tested for homogeneous concentration, and planar random rod orientations at the inlet (Dirichlet BC6 $A_{11}/c = A_{22}/c = 0.5$ and $A_{12}/c = 0$). Figures 17 and 19 show the concentration results of rods in the channel for quadratic and IBOF closures, respectively. Figures 18 and 20 show the orientation

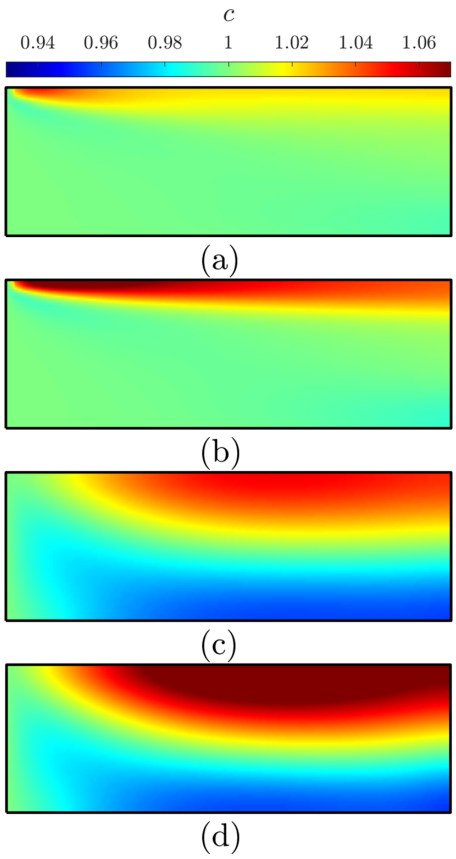

FIG. 19. Concentration distribution c results using the IBOF closure approximation, across the planar channel, where homogeneous concentration and random orientation of the rods are prescribed at the inlet for (a) $\mathrm{Pe}_r = 10$, $\mathrm{Pe}_\perp = 10^3$; (b) $\mathrm{Pe}_r = 10^3$, $\mathrm{Pe}_\perp = 10^3$; (c) $\mathrm{Pe}_r = 10$, $\mathrm{Pe}_\perp = 10$; and (d) $\mathrm{Pe}_r = 10^3$, $\mathrm{Pe}_\perp = 10$.

component A_{11}/c using the mentioned closures. These figures show a quantitative agreement between the full solution of the FP equation and the macromodel; nevertheless, the use of the closure approximations. Tables I and II show the maximum and mean absolute error percentage values along the channel for concentration c and orientation component A_{11}/c, respectively. The IBOF closure provides an excellent agreement for the concentration and orientation, better than the quadratic. For IBOF, the errors with respect to the solutions obtained solving the FP equation [Eq. (16)] across the channel does not exceed 5% for both concentration and orientation component A_{11}/c for the tested cases (Tables I and II), while the mean absolute errors are much lower than the error values obtained using the quadratic closure. These results further demonstrate the validity of the derived macromodel also for nonhomogeneous systems. The mean absolute error is affected by Pe_r and $\mathrm{Pe}_\perp$. The tested cases using the quadratic closure show that the mean absolute errors for both orientation and concentration increase with decreasing the rotary and the perpendicular Peclet numbers. While for IBOF, the relation between the Peclet numbers and the mean absolute errors is unclear.

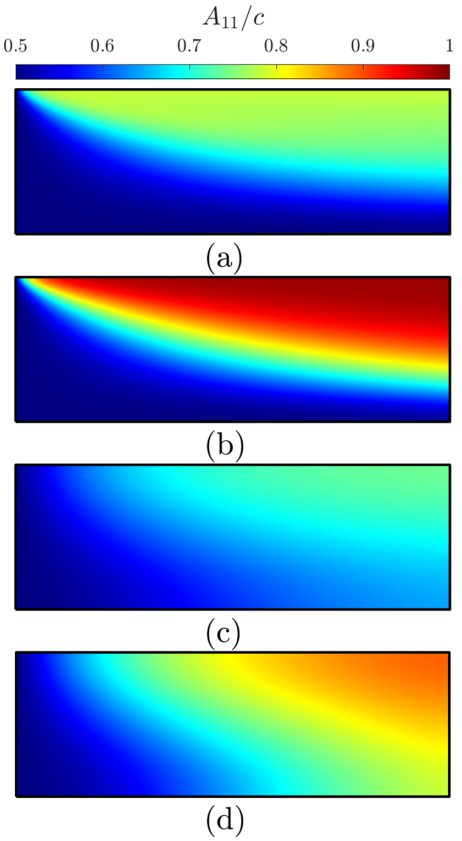

FIG. 20. Orientation component A_{11}/c results using the IBOF closure approximation, across the planar channel, where homogeneous concentration and random orientation of the rods are prescribed at the inlet for (a) $\mathrm{Pe}_r = 10$, $\mathrm{Pe}_\perp = 10^3$; (b) $\mathrm{Pe}_r = 10^3$, $\mathrm{Pe}_\perp = 10^3$; (c) $\mathrm{Pe}_r = 10$, $\mathrm{Pe}_\perp = 10$; and (d) $\mathrm{Pe}_r = 10^3$, $\mathrm{Pe}_\perp = 10$.

TABLE I. Values of the maximum percentage error and the mean absolute percentage error for concentration c, $\mathrm{CE}_{\mathrm{max}}$ and $\mathrm{CE}_{\mathrm{mean}}$, respectively, using the IBOF and quadratic closures with respect to the results in method 1.

	Percentage error of concentration c (CE)			
	IBOF closure		Quadratic closure	
	$\mathrm{CE}_{\mathrm{max}}$	$\mathrm{CE}_{\mathrm{mean}}$	$\mathrm{CE}_{\mathrm{max}}$	$\mathrm{CE}_{\mathrm{mean}}$
$\mathrm{Pe}_r = 10$ $\mathrm{Pe}_\perp = 10^3$	4.89%	2.45%	7.08%	3.94%
$\mathrm{Pe}_r = 10^3$ $\mathrm{Pe}_\perp = 10^3$	4.62%	0.42%	5.88%	0.46%
$\mathrm{Pe}_r = 10$ $\mathrm{Pe}_\perp = 10$	4.14%	1.39%	6.38%	2.46%
$\mathrm{Pe}_r = 10^3$ $\mathrm{Pe}_\perp = 10$	4.24%	0.28%	5.27%	0.44%

TABLE II. Values of the maximum percentage error and the mean absolute percentage error for orientation component A_{11}/c, OE_{max} and OE_{mean}, respectively, using the IBOF and quadratic closures with respect to the results in method 1.

	Percentage error of orientation A_{11}/c (OE)			
	IBOF closure		Quadratic closure	
	OE_{max}	OE_{mean}	OE_{max}	OE_{mean}
$Pe_r = 10$ $Pe_\perp = 10^3$	3.07%	1.31%	16.01%	6.62%
$Pe_r = 10^3$ $Pe_\perp = 10^3$	3.17%	0.29%	14.92%	5.3%
$Pe_r = 10$ $Pe_\perp = 10$	1.7%	0.78%	14.45%	7.32%
$Pe_r = 10^3$ $Pe_\perp = 10$	2.21%	0.84%	13.51%	6.56%

V. CONCLUSION

The major contribution of this work is the derivation of a macromodel to investigate the flow of Brownian particle suspensions taking into account the coupling between the concentration and the orientation of particles. Such macromodel reduces drastically (by a factor 13) the computational time required to numerically solve a full FP equation for the 2D case explored here. The effect of anisotropic translational diffusion, depending on the orientation, is studied in a planar channel with and without the presence of a circular obstacle. The Brownian translational diffusion favors the rod migrations toward the walls. The concentration gradient does not affect the orientation of rods, but it favors their migration. Aligned rods are slower to migrate than planar random ones. These results are in qualitative agreement with the results in the literature. A circular obstacle in a planar channel causes complexity in the flow field which affects the rod suspensions. The macromodel is verified based on the solution of the Fokker-Planck equation. Future works will focus in exploring the effect between particle and Brownian stresses, the stress terms will be developed and added to Stokes equation as in the work of Saintillan and Shelley [43]. On the other hand, the effect of anisotropic translational diffusion in the case of active particles will be investigated.

ACKNOWLEDGMENTS

H.I. particularly wishes to acknowledge the Brittany Region and ISblue for their financial supports. G.N. acknowledges financial support from the Natural Sciences and Engineering Research Council of Canada (NSERC) (RGPIN-2017-03783).

APPENDIX A: DERIVATION FOR THE EQUATION OF CHANGE OF A_2

This part focuses on the derivation of Eq. (9). First, Eq. (5) is multiplying with the tensor $\mathbf{pp}/V$ and integrating over all orientations and the spatial domain to give

$$\frac{1}{V}\int_{\mathbf{p}}\int_{\mathbf{r}_c}\frac{D\Psi}{Dt}\mathbf{pp}d\mathbf{r}_c d\mathbf{p} = \frac{1}{V}\int_{\mathbf{p}}\int_{\mathbf{r}_c}\nabla_{\mathbf{x}}\cdot(\mathbf{D}_t\cdot\nabla_{\mathbf{x}}\Psi)\mathbf{pp}d\mathbf{r}_c d\mathbf{p} - \frac{1}{V}\int_{\mathbf{p}}\int_{\mathbf{r}_c}\nabla_{\mathbf{p}}\cdot(\dot{\mathbf{p}}_j\Psi)\mathbf{pp}d\mathbf{r}_c d\mathbf{p} + \frac{D_r}{V}\int_{\mathbf{p}}\int_{\mathbf{r}_c}\nabla_{\mathbf{p}}^2\Psi\mathbf{pp}d\mathbf{r}_c d\mathbf{p}. \quad \text{(A1)}$$

The left-hand side of the above equation is simply the material derivative of $\mathbf{A}_2$, i.e., $D\mathbf{A}_2/Dt$. The first term on the right-hand side of Eq. (A1) has already been addressed in Eq. (8). As for the second term on the right-hand side of Eq. (A1), application of the integration by parts formula leads to [40]

$$-\frac{1}{V}\int_{\mathbf{p}}\int_{\mathbf{r}_c}\nabla_{\mathbf{p}}\cdot(\dot{\mathbf{p}}_j\Psi)\mathbf{p}\mathbf{p}d\mathbf{r}_c d\mathbf{p} = -\frac{1}{2}(\boldsymbol{\omega}\cdot\mathbf{A}_2 - \mathbf{A}_2\cdot\boldsymbol{\omega}) + \frac{\lambda}{2}(\dot{\boldsymbol{\gamma}}\cdot\mathbf{A}_2 + \mathbf{A}_2\cdot\dot{\boldsymbol{\gamma}} - 2\mathbf{A}_4:\dot{\boldsymbol{\gamma}}). \quad \text{(A2)}$$

In obtaining the above equation, the Jeffery's equation [Eq. (4)] has been used. Finally, the integration by parts formula is applied two times in the last term of Eq. (A1) to yield [40]

$$\frac{D_r}{V}\int_{\mathbf{p}}\int_{\mathbf{r}_c}\nabla^2_{\mathbf{p}}\Psi\mathbf{p}\mathbf{p}d\mathbf{r}_c d\mathbf{p} = 2D_r(c\boldsymbol{\delta} - \alpha\mathbf{A}_2), \quad \text{(A3)}$$

where α equals 2 in 2D and 3 in 3D. Gathering these results together, we obtain the expression for the material derivative of $\mathbf{A}_2$ given in Eq. (9).

APPENDIX B: NUMERICAL METHOD

For this work, two different numerical methods have been used. The first problem is to solve the FP equation [Eq. (5)] in a direct numerical computation. This numerical model is referred by method 1 in this article. While the other method is demonstrated to compute the macromodel ($\mathbf{A}_2$) by solving the partial differential equation of evolution of $\mathbf{A}_2$ [Eq. (9)]. This numerical model is referred by method 2 in this article. For both problems, the finite-element method is applied. Utilized software is COMSOL Multiphysics 5.5 to solve the problems including the fluid flow field, and the partial differential equations.

1. Method 1

In order to solve the FP equation for Ψ [Eq. (16)] for particle orientation and concentration in 2D, a numerical model is composed of two components (a model component in COMSOL Multiphysics is a fundamental section of the model that includes a geometry, physics interface, mesh, variables, and other definitions that are specific to that component), a 2D component and a 3D component. Benefiting from the COMSOL advantage of linear extrusion coupling operator which maps an expression defined on a source to an expression that can be evaluated in the destination (mapping two different components), and general projection operator, which integrates along curves defined via expressions that can be Cartesian coordinates. Component 1 is a 2D rectangular geometry, the creeping flow is defined by solving Eqs. (19) and (20) and with the given boundary conditions, the spatial discretization of the pressure and velocity fields are done on P1 + P2 element. Component 2 is a 3D rectangular block, the base rectangle has the dimensions as component 1, and the horizontal coordinates are defined as spatial coordinates, where component 1 is extruded, while the vertical coordinate are defined as the discretization of ϕ, considering ϕ is the angle of orientation of the particle. $\phi = 0$ means the rod is aligned in the direction of flow since the rods are symmetry, so the head of the rod is identical to its tail. ϕ is discretized from 0 to π, respecting the periodic conditions of symmetric particles

$$\Psi(\mathbf{r}_c, \phi, t) = \Psi(\mathbf{r}_c, \phi + \pi, t). \quad \text{(B1)}$$

Equation (16) is then projected in the ϕ direction to yield for

$$\frac{D\Psi}{Dt} = \nabla_{\mathbf{x}}\cdot(\mathbf{D}_t\cdot\nabla_{\mathbf{x}}\Psi) - \nabla_{\phi}\cdot(\mathbf{p}_j\Psi) + \frac{1}{\mathrm{Pe}_r}\nabla^2_{\phi}\Psi, \quad \text{(B2)}$$

knowing that ∇_ϕ is the gradient operator in the direction of ϕ. Elements with Lagrangian shape functions of order quadratic are used for Ψ.

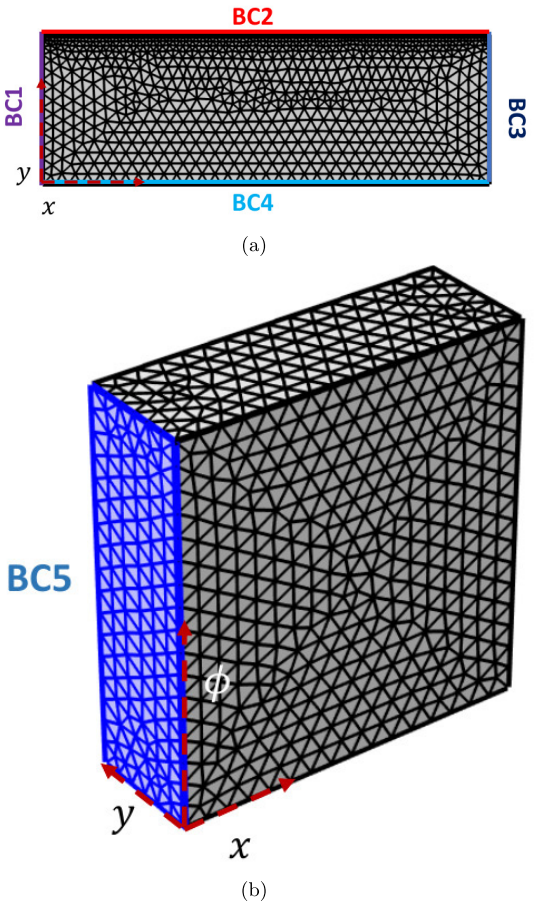

FIG. 21. FE mesh for components 1 and 2 in method 1. BC1, creeping inflow; BC2, No slip condition; BC3, pressure outlet; BC4, symmetry condition; and BC5, Dirichlet condition for Ψ. (a) Component 1. (b) Component 2.

All the computations were carried out on a workstation Dell PowerEdge R930 with Intel Xeon E7-8860 v4 @ 2.20 GHz CPU with 72 threads and 1TB RAM. The computation was around 3 h and 36 minutes in each case for the three Peclet regimes. The used mesh for component 1 is COMSOL's predefined free triangular mesh of fine resolution of 3852 elements. While for component 2, it is free tetrahedral of coarser size, with scale geometry of 9 in the x, y, and ϕ directions of 552 663 and 17 064 tetrahedral and triangular elements, respectively.

2. Method 2

The second model is composed of a 2D rectangular channel, with the given boundary conditions BC2, BC3, and BC4, while BC6 is the inlet flow velocity in addition to the Dirichlet boundary conditions for $\mathbf{A}_2$ (see Fig. 22). The model is composed of two physics, one for solving the creeping flow, and the other is a coefficient partial differential equations, for solving the evolution of $\mathbf{A}_2$ (A_{11}, A_{12}, and A_{22}). In this model, Eqs. (18), (19), and (20) are solved using quadratic and IBOF closures [47,49]. All the computations were carried out on a laptop HP EliteBook 8570p with Intel core i7 and 8 GB RAM. The computation was around 16 min in each case for the three Peclet regimes. The used mesh is the COMSOL's predefined free triangular mesh of fine resolution of 3852 elements.

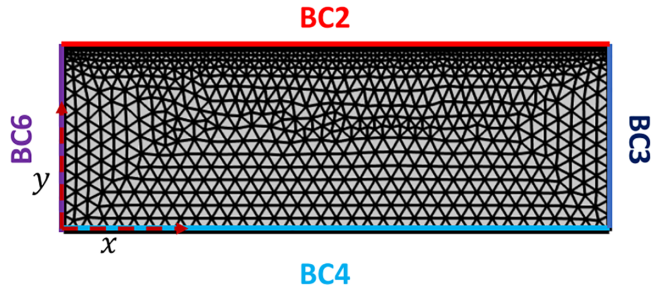

FIG. 22. FE mesh for model 2 BC2: No slip condition, BC3: pressure outlet, BC4: symmetry condition, BC6: creeping inflow + Dirichlet BC for $\mathbf{A}_2$.

3. Numerical precision

The dimensionless Fokker-Planck equation can be written as

$$\mathrm{Pe}_\perp \mathbf{u}\cdot\nabla_{\mathbf{x}}\Psi - \mathrm{Pe}_\perp \nabla_{\mathbf{x}}\cdot(\mathbf{D}_t\cdot\nabla_{\mathbf{x}}\Psi) + \mathrm{Pe}_\perp \nabla_{\mathbf{p}}\cdot(\dot{\mathbf{p}}_j\Psi) - \frac{\mathrm{Pe}_\perp}{\mathrm{Pe}_r}\nabla^2_{\mathbf{p}}\Psi = 0. \tag{B3}$$

It is important to study the precision of a new numerical simulation. After each computation, the normalization of the probability distribution function and the bulk concentration at the outlet is obtained, and the error is calculated. Figure 23 shows the error calculated from the numerical normalization of Ψ with the exact one. It is found that at high and low translational diffusions, the error is between 1% and 2%, which is acceptable. The highest error is at $\mathrm{Pe}_\perp = 1$. Numerical instabilities in COMSOL Multiphysics occur when the element Peclet number exceeds 1. Element Peclet number relates the convective term, element mesh size, and the diffusion term. An element Peclet number greater than one is caused by either large convective or small diffusive activity for an acceptable mesh element size. In this work, two element Peclet numbers are found, spatial (relating

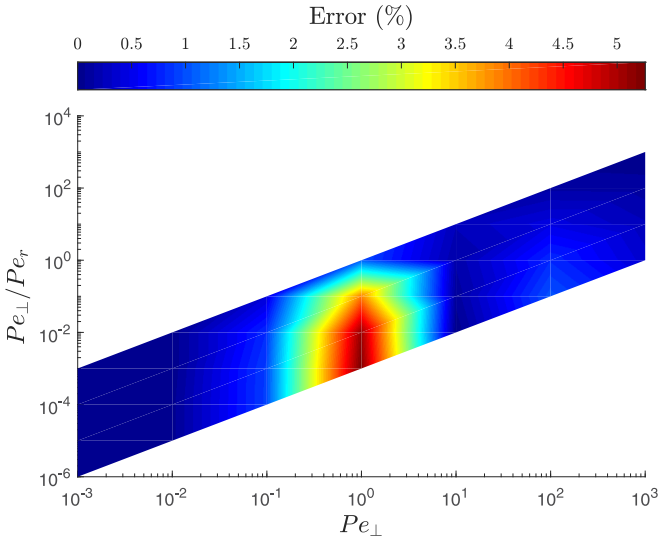

FIG. 23. Percentage of the numerical errors calculated from the normalization of Ψ, for the case of planar channel with homogeneous concentration and planar random orientation at the inlet as a function of Peclet numbers.

the spatial diffusion with spatial convection) [59] and configurational (relating the rotary diffusion with rotary convection).

For low $Pe_{\perp}$, diffusion is dominant in this case, the model is stable, and element Peclet numbers are less than 1. For high $Pe_{\perp}$, spatial convection is dominant, in this case, stabilization in the spatial domain is considered by COMSOL (streamline and crosswind diffusion). For $Pe_{\perp} = 1$, the spatial element Peclet number is less than 1, while the configurational one equals the rotary Peclet number, which is greater than 1. In this case, the COMSOL's stabilization is not implemented.

[1] S. Houshyar, R. A. Shanks, and A. Hodzic, The effect of fiber concentration on mechanical and thermal properties of fiber-reinforced polypropylene composites, J. Appl. Polym. Sci. **96**, 2260 (2005).

[2] J. L. Thomason and W. M. Groenewoud, The influence of fibre length and concentration on the properties of glass fibre reinforced polypropylene: 2. Thermal properties, Compos. A: Appl. Sci. Manufact. **27**, 555 (1996).

[3] M. Li, Z. Ali, X. Wei, L. Li, G. Song, X. Hou, H. Do, J. C. Greer, Z. Pan, C. T. Lin *et al.*, Stress induced carbon fiber orientation for enhanced thermal conductivity of epoxy composites, Compos. B: Eng. **208**, 108599 (2021).

[4] G. B. Jeffery, The motion of ellipsoidal particles immersed in a viscous fluid, Proc. R. Soc. Lond. A **102**, 161 (1922).

[5] M. Rahnama, D. L. Koch, Y. Iso, and C. Cohen, Hydrodynamic, translational diffusion in fiber suspensions subject to simple shear flow, Phys. Fluids **5**, 849 (1993).

[6] C. A. Stover, D. L. Koch, and C. Cohen, Observations of fibre orientation in simple shear flow of semi-dilute suspensions, J. Fluid Mech. **238**, 277 (1992).

[7] F. Folgar and C. L. Tucker III, Orientation behavior of fibers in concentrated suspensions, J. Reinf. Plast. Compos. **3**, 98 (1984).

[8] E. J. Hinch and L. G. Leal, Rotation of small non-axisymmetric particles in a simple shear flow, J. Fluid Mech. **92**, 591 (1979).

[9] A. L. Yarin, O. Gottlieb, and I. V. Roisman, Chaotic rotation of triaxial ellipsoids in simple shear flow, J. Fluid Mech. **340**, 83 (1997).

[10] J. Einarsson, B. M. Mihiretie, A. Laas, S. Ankardal, J. R. Angilella, D. Hanstorp, and B. Mehlig, Tumbling of asymmetric microrods in a microchannel flow, Phys. Fluids **28**, 013302 (2016).

[11] A. Hijazi and A. Khater, Brownian dynamics simulations of rigid rod-like macromolecular particles flowing in bounded channels, Comput. Mater. Sci. **22**, 279 (2001).

[12] M. Zurita-Gotor, J. Bławzdziewicz, and E. Wajnryb, Motion of a rod-like particle between parallel walls with application to suspension rheology, J. Rheol. **51**, 71 (2007).

[13] A. Atwi, A. Khater, and A. Hijazi, Three-dimensional simulations for the dynamics of dilute colloidal suspensions of ellipsoidal-like particles flowing in the bulk and near solid boundaries, Polymer **54**, 1555 (2013).

[14] E. Holmstedt, H. O. Åkerstedt, T. Staffan Lundström, and S. M. Högberg, Modeling transport and deposition efficiency of oblate and prolate nano-and micro-particles in a virtual model of the human airway, J. Fluids Eng. **138**, 081203 (2016).

[15] S. Monjezi, J. D. Jones, A. K. Nelson, and J. Park, The effect of weak confinement on the orientation of nanorods under shear flows, Nanomaterials **8**, 130 (2018).

[16] D. Z. Gunes, R. Scirocco, J. Mewis, and J. Vermant, Flow-induced orientation of non-spherical particles: Effect of aspect ratio and medium rheology, J. Non-Newton. Fluid Mech. **155**, 39 (2008).

[17] J. Férec, E. Bertevas, B. C. Khoo, G. Ausias, and N. Phan-Thien, Rigid fiber motion in slightly non-Newtonian viscoelastic fluids, Phys. Fluids **33**, 103320 (2021).

[18] J. G. Kirkwood and P. L. Auer, The visco-elastic properties of solutions of rod-like macromolecules, J. Chem. Phys. **19**, 281 (1951).

[19] M. Doi and S. F. Edwards, *The Theory of Polymer Dynamics*, Vol. 73 (Oxford University Press, Oxford, 1988).
[20] P. L. Frattini and G. G. Fuller, Rheo-optical studies of the effect of weak Brownian rotations in sheared suspensions, J. Fluid Mech. **168**, 119 (1986).
[21] D. Xie, M. Lista, G. G. Qiao, and D. E. Dunstan, Shear induced alignment of low aspect ratio gold nanorods in Newtonian fluids, J. Phys. Chem. Lett. **6**, 3815 (2015).
[22] E. J. Hinch and L. G. Leal, Time-dependent shear flows of a suspension of particles with weak Brownian rotations, J. Fluid Mech. **57**, 753 (1973).
[23] A. Hijazi and M. Zoaeter, Brownian dynamics simulations for rod-like particles in dilute flowing solution, Eur. Polym. J. **38**, 2207 (2002).
[24] B. D. Leahy, D. L. Koch, and I. Cohen, The effect of shear flow on the rotational diffusion of a single axisymmetric particle, J. Fluid Mech. **772**, 42 (2015).
[25] D. Palanisamy and W. K. den Otter, Efficient Brownian dynamics of rigid colloids in linear flow fields based on the grand mobility matrix, J. Chem. Phys. **148**, 194112 (2018).
[26] A. Zöttl, K. E. Klop, A. K. Balin, Y. Gao, J. M. Yeomans, and D. G. Aarts, Dynamics of individual Brownian rods in a microchannel flow, Soft Matter **15**, 5810 (2019).
[27] A. Lozinski and C. Chauviere, A fast solver for Fokker-Planck equation applied to viscoelastic flows calculations: 2D FENE model, J. Comput. Phys. **189**, 607 (2003).
[28] C. Chauviere and A. Lozinski, Simulation of complex viscoelastic flows using theFokker-Planck equation: 3D FENE model, J. Non-Newton. Fluid Mech. **122**, 201 (2004).
[29] A. Moosaie and M. Manhart, A direct numerical simulation method for flow of Brownian fiber suspensions in complex geometries, J. Dispers. Sci. Technol. **34**, 427 (2013).
[30] P. J. Krochak, J. A. Olson, and D. M. Martinez, Fiber suspension flow in a tapered channel: The effect of flow/fiber coupling, Int. J. Multiphase Flow **35**, 676 (2009).
[31] A. Ammar, B. Mokdad, F. Chinesta, and R. Keunings, A new family of solvers for some classes of multidimensional partial differential equations encountered in kinetic theory modeling of complex fluids, J. Non-Newton. Fluid Mech. **139**, 153 (2006).
[32] A. Ammar, B. Mokdad, F. Chinesta, and R. Keunings, A new family of solvers for some classes of multidimensional partial differential equations encountered in kinetic theory modelling of complex fluids: Part ii: Transient simulation using space-time separated representations, J. Non-Newton. Fluid Mech. **144**, 98 (2007).
[33] D. Mezi, G. Ausias, S. G. Advani, and J. Férec, Fiber suspension in 2D nonhomogeneous flow: The effects of flow/fiber coupling for Newtonian and power-law suspending fluids, J. Rheol. **63**, 405 (2019).
[34] J. M. Park and S. J. Park, Modeling and simulation of fiber orientation in injection molding of polymer composites, Math. Probl. Eng. **2011**, 1 (2011).
[35] J. Férec, G. Ausias, M. C. Heuzey, and P. J. Carreau, Modeling fiber interactions in semiconcentrated fiber suspensions, J. Rheol. **53**, 49 (2009).
[36] R. L. Schiek and E. S. G. Shaqfeh, Cross-streamline migration of slender Brownian fibres in plane Poiseuille flow, J. Fluid Mech. **332**, 23 (1997).
[37] L. C. Nitsche and E. J. Hinch, Shear-induced lateral migration of Brownian rigid rods in parabolic channel flow, J. Fluid Mech. **332**, 1 (1997).
[38] J. Park, J. M. Bricker, and J. E. Butler, Cross-stream migration in dilute solutions of rigid polymers undergoing rectilinear flow near a wall, Phys. Rev. E **76**, 040801 (2007).
[39] O. Z. Sharaf, A. N. Al-Khateeb, D. C. Kyritsis, and E. Abu-Nada, Numerical investigation of nanofluid particle migration and convective heat transfer in microchannels using an Eulerian-Lagrangian approach, J. Fluid Mech. **878**, 62 (2019).
[40] S. G. Advani and C. L. Tucker III, The use of tensors to describe and predict fiber orientation in short fiber composites, J. Rheol. **31**, 751 (1987).
[41] R. J. Phillips, R. C. Armstrong, R. A. Brown, A. L. Graham, and J. R. Abbott, A constitutive equation for concentrated suspensions that accounts for shear-induced particle migration, Phys. Fluids **4**, 30 (1992).
[42] N. C. Shapley, R. C. Armstrong, and R. A. Brown, Laser doppler velocimetry measurements of particle velocity fluctuations in a concentrated suspension, J. Rheol. **46**, 241 (2002).

[43] D. Saintillan and M. J. Shelley, Active suspensions and their nonlinear models, C. R. Phys. **14**, 497 (2013).
[44] S. Weady, M. J. Shelley, and D. B. Stein, A fast chebyshev method for the Bingham closure with application to active nematic suspensions, J. Comput. Phys. **457**, 110937 (2022).
[45] T. Sanchez, D. T. Chen, S. J. DeCamp, M. Heymann, and Z. Dogic, Spontaneous motion in hierarchically assembled active matter, Nature **491**, 431 (2012).
[46] S. M. Dinh and R. C. Armstrong, A rheological equation of state for semiconcentrated fiber suspensions, J. Rheol. **28**, 207 (1984).
[47] S. G. Advani and C. L. Tucker III, Closure approximations for three-dimensional structure tensors, J. Rheol. **34**, 367 (1990).
[48] J. S. Cintra Jr and C. L. Tucker III, Orthotropic closure approximations for flow-induced fiber orientation, J. Rheol. **39**, 1095 (1995).
[49] D. H. Chung and T. H. Kwon, Invariant-based optimal fitting closure approximation for the numerical prediction of flow-induced fiber orientation, J. Rheol. **46**, 169 (2002).
[50] H. C. Tseng, R. Y. Chang, and C. H. Hsu, Cross-streamline migration of slender Brownian fibres in plane Poiseuille flow, J. Rheol. **62**, 313 (2018).
[51] B. Ezhilan, M. J. Shelley, and D. Saintillan, Instabilities and nonlinear dynamics of concentrated active suspensions, Phys. Fluids **25**, 070607 (2013).
[52] J. Férec, M. Heniche, M. C. Heuzey, G. Ausias, and P. J. Carreau, Numerical solution of the Fokker-Planck equation for fiber suspensions: Application to the Folgar–Tucker–Lipscomb model, J. Non-Newtonian Fluid Mech. **155**, 20 (2008).
[53] S. B. Chen and L. Jiang, Orientation distribution in a dilute suspension of fibers subject to simple shear flow, Phys. Fluids **11**, 2878 (1999).
[54] Y. Du, H. Jiang, and Z. Hou, Study of active Brownian particle diffusion in polymer solutions, Soft Matter **15**, 2020 (2019).
[55] D. Ghernaout, A. I. Al-Ghonamy, B. Boucherit, A.and Ghernaout, M. W. Naceur, N. A. Messaoudene, M. Aichouni, A. A. Mahjoubi, and N. A. Elboughdiri, Brownian motion and coagulation process, Am. J. Environ. Prot. **4**, 1 (2015).
[56] H. Haddadi, S. Shojaei-Zadeh, K. Connington, and J. F. Morris, Suspension flow past a cylinder: Particle interactions with recirculating wakes, J. Fluid Mech. **760** (2014).
[57] N. Phan-Thien and A. L. Graham, A new constitutive model for fibre suspensions: Flow past a sphere, Rheol. Acta **30**, 44 (1991).
[58] G. Kumar and G. Natale, Settling dynamics of two spheres in a suspension of brownian rods, Phys. Fluids **31**, 073104 (2019).
[59] S. Fabrice, Understanding stabilization methods https://www.comsol.com/blogs/understanding-stabilization-methods/.